

Statistically determined dispersion relations of magnetic field fluctuations in the terrestrial foreshock

B. Hnat¹, D. O'Connell¹, V. M. Nakariakov¹

¹ *Centre for Fusion, Space and Astrophysics, University of Warwick.*

(Dated: February 1, 2016)

We obtain dispersion relations of magnetic field fluctuations for two crossings of the terrestrial foreshock by Cluster spacecraft. These crossings cover plasma conditions which differ significantly in their plasma β but not in the properties of the encountered ion population, both showing shell-like distribution function. Dispersion relations are reconstructed using two-point instantaneous wave number estimations from pairs of Cluster spacecraft. The accessible range of wave vectors, limited by the available spacecraft separations, extends to $\approx 2 \times 10^4$ km. Results show multiple branches of dispersion relation, associated with different power of magnetic field fluctuations. We find that Sunward propagating fast magnetosonic waves and beam resonant modes are dominant for the high plasma β interval, while the dispersions of magnetically dominated interval include Alfvén and fast magnetosonic modes propagating Sunward and unit-Sunward.

PACS numbers:

I. INTRODUCTION.

The region upstream of the terrestrial bow shock provides a testbed for a large number of generic plasma processes, from Fermi acceleration [1] and shock reformation [2] to a wide range of instabilities [3]. Due to the collisionless nature of the solar wind plasma, the kinetic energy of the upstream flow is converted into heat by complex interactions of particles with fluctuations and through particle reflection (acceleration) at the shock [4, 5]. This leads to non-thermal velocity distribution functions upstream of the shock and these can become linearly unstable to small perturbations, resulting in large amplitude fluctuations in the magnetic field and other plasma parameters. Scattering and heating of ions by such fluctuations is of great importance to understanding the channels of momentum and energy exchange in the system. It is essential to keep in mind that the upstream flow is not laminar and that large amplitude, nearly harmonic fluctuations coexist with turbulent solar wind. Identification of frequencies where the turbulent energy transfer becomes dominant is of great importance to the determination of wave-particle interaction processes.

The unperturbed solar wind plasma near the Earth's orbit shows correlations between velocity and magnetic field fluctuations, characteristic of transverse Alfvén mode [10]. The phase coherence of these fluctuations is usually destroyed prior to their arrival at the foreshock, and only a single observation of pure Alfvénic mode at 1AU has been reported [9] to date. Small density perturbations are also detected in the unperturbed solar wind and these are a mixture of the pressure-balanced structures of coronal origin and fast magnetosonic modes [8]. The ion cyclotron waves, Alfvén waves with frequency near the ion cyclotron frequency and with the field-aligned wave vector, have been suggested as a possible source of solar wind heating and acceleration, but unambiguous detection of these waves in the solar wind

has been elusive, see for example [11]. Upon entering the foreshock, the solar wind plasma interacts with the small population of reflected particles and this interaction modifies kinetic properties of the plasma and can lead to a significantly different dynamics.

Few classes of ion velocity distribution functions have been observed in the terrestrial foreshock [6] and, in the case of the quasi-parallel ($\Theta_{B,n} < 45^\circ$) bow shock, these distributions have been associated with low frequency electromagnetic fluctuations. Fast magnetosonic waves, travelling in the direction of the beam, are the fastest grown unstable modes destabilised by the cold and tenuous beam-like distributions, corresponding to ions travelling Sunward and nearly parallel to the background magnetic field. For sufficiently dense and warm beam the destabilised fast wave can also propagate against the beam [21]. In addition to the beam-like distributions there are also these of “diffuse” type [6, 7], which are nearly isotropic in the phase space, and have large temperatures, sometimes exceeding 10 keV. Enhanced wave activity has been observed for these distributions, with both left and right-hand modes competing in growth rates, in numerical simulations with different beam and plasma parameters [22]. We note the importance of minor ions, especially Helium He^{++} , which may resonate with the left-hand mode at low frequencies, where the power of fluctuations tends to be greater and provide energy source for magneto acoustic cyclotron instability [38]. In principle, the range of frequencies supported by

TABLE I: Cluster intervals parameters.

Interval	χ [km]	\mathbf{B} [nT, GSE]	$\langle V_{sw} \rangle$	β	V_A	$\Theta_{V,B}$	ω_{cp}	ρ_i [km]
I1	70.5	(-6.9, 0.3, 1.3)	315.5	0.4	60.5	21	0.7	42.1
I2	82.3	(7.9, -3.9, 4.7)	406.6	3.2	93.0	147	1.0	177.5

foreshock plasmas span many orders of magnitude, from ultra-low frequency (ULF) waves at about 10^{-2} Hz to electron Langmuir waves at hundreds of kHz. A sub-

stantial experimental literature exists, where the dominant modes at low frequencies have been characterised in terms of their wave properties in different regions of the terrestrial foreshock [16, 17, 19, 20]. The focus on ULF waves is motivated by numerical simulations [18, 22, 30], which established that, for realistic plasma parameters, beam-like distributions generate electromagnetic fluctuations in the low frequency range, that is, below the ion cyclotron frequency. More recent work took into account other plasma parameters, and their correlations with the magnetic field fluctuations, providing more unambiguous identification of magnetohydrodynamic (MHD) modes (e.g., [33]).

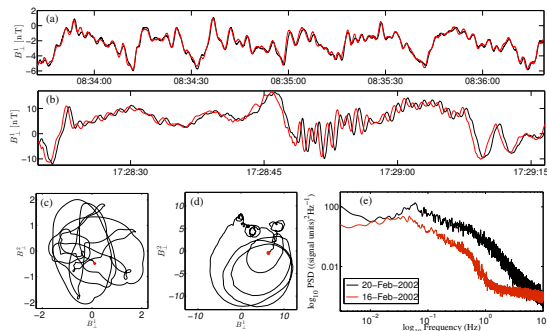


FIG. 1: Magnetic field data summary for two time intervals. Panel (a): transverse magnetic field component associated with the largest eigenvalue of the minimum variance analysis for a section within *I1* and for spacecraft *C3* (black trace) and *C4* (red trace). Panel (b): same as (a) for the interval *I2*. Panels (c,d): hodograms of the transverse magnetic field components for selected short subintervals in *I1* and *I2*, respectively. Panel (e) power spectral density for B_{\perp}^1 component of interval *I1* (red) and interval *I2* (black).

Multi-point Cluster observations, aided with the wave telescope technique, provided estimates of the dispersion relations associated with the dominant modes in the low frequency range and clearly demonstrated the existence of Sunward propagating waves, broadly consistent with the ion beam instability as a generation mechanism [14]. Given the multiple locations where unstable distributions may exist, the growth rates of relevant instabilities (order 100 seconds) and the speed of the propagation (typically 50-100 km/s) one expects a continuous distribution of power for unstable modes [22]. In addition, nonlinear processes, for example, decay instability of Alfvén waves or/and the modulation instability of the fast magnetosonic mode [25], may lead to the re-distributed of power.

Our purpose in this work is to apply a new technique, which clearly identifies how fluctuating power is distributed among different quasi-coherent modes in two foreshock plasmas, which differ in their macroscopic parameters, but have similar ion distributions. This work extends previous multi-point studies by applying a statistical method [26], capable of detecting dispersion re-

lations associated with different coexisting modes within the same set of fluctuations. Each time interval is treated as a set of independent shorter realisations, each contributing to a statistically generated dispersion relation represented as the cumulative power at each identified frequency and the corresponding wave number. We find that, for anisotropic and warm beam, the most energetic fluctuations are located on at the right-hand polarised mode and resonant ion beam branches of the dispersion relation. A smaller, but considerable, amount of power, is also found in the left-hand polarised branch, which extends to large modules of wave number, $k\rho_p \sim 0.75$. For the interval with diffuse-like ion distribution we find the dominant power at low frequencies to be associated with coherent structures, which may correspond to turbulent vortices with slow dynamics, that is, dominated by advective solar wind transport.

II. DATA.

The dataset consists of two foreshock crossings, 16/02/2002 at 07:50-09:20 and 20/02/2002 at 16:56-17:56, hereafter referred to as *I1* and *I2*, respectively. These foreshock crossings were selected based on the clear presence of wave modes in frequency spectra as well as for the small spacecraft separation of the spacecraft pair *C3* and *C4*. We use magnetic field data from the FGM instrument [23] with sampling frequency of ≈ 22.5 Hz and spin resolution (4 seconds) CIS-HIA data [24] for plasma parameters. Table I presents a summary of the plasma parameters for both intervals. We note a large difference in ion plasma β_i for these intervals as well as a different direction of the main component of the magnetic field (GSE x direction). For the interval *I1* the magnetic field is directed towards the Earth, while interval *I2* has magnetic field pointing Sunwards. Both intervals has been studied before in the context of ULF waves [13–15] and their possible impact on temperature anisotropy of the core ion population [32].

Our analysis is undertaken for transverse fluctuations of the magnetic field expressed in minimum variance coordinates. The ratio of the intermediate and minimum eigenvalues was ~ 2.5 , which we contribute to the non-stationary character of these considerably long intervals. Figure 1 presents a summary of the magnetic field data for the two intervals. These intervals show typical values of the ion number density ($\langle n_p \rangle \sim 5 - 10 \text{ cm}^{-3}$) of the solar wind and their bulk speed puts them in the slow solar wind category. Clear wave trains are seen in panels (a,b), in which we plot snapshots of the transverse magnetic field component corresponding to the highest eigenvalue of minimum variance analysis. Two traces show data from spacecrafts *C3* (black) and *C4* (red). These demonstrate that the observed temporal shift between the signals is never larger than a period of a wave. Panels (c,d) demonstrate that, for sufficiently short subintervals, a unique sense of circular polarisation can be established

in the spacecraft frame. While interval *I2* shows fairly consistent left-hand polarisation, interval *I1* exhibits frequent changes from left to right-hand polarisation. The frequency spectra of transverse magnetic field components, shown in panel (e), reveal peaks at frequencies lower than the proton gyro-frequency ($0.01 \leq \nu \leq 0.1$ Hz) and a broadband, power law behaviour at higher frequencies for both intervals. The proton cyclotron frequency in the spacecraft frame has been estimated at $\nu_{cp} \approx 0.11$ Hz, but a large Doppler shift puts it in the range of 3–5 Hz in the plasma frame. Table I, gives values of gyro frequencies (angular frequencies, in [rad/s]) in the plasma frame of reference.

III. METHODOLOGY.

Transverse magnetic field components, from spacecrafts *C3* and *C4* are used to construct an estimate of the dispersion relation. We use a Fourier technique based on Beall's algorithm [26–28] designed for fixed probe pairs. Let (x, t) represent a zero-mean, stationary, homogeneous vector field, which can be represented as a superposition of plane waves, that is,

$$B(x, t) = \int_{-\infty}^{\infty} dk \int_{-\infty}^{\infty} \tilde{B}(k, \omega) \exp[i(k \cdot x - \omega t)], \quad (1)$$

where the integrals are taken as the discrete sum of the measurements. The goal is to calculate an estimate of the dispersion relation, $k = k(\omega)$, which in the case of two probes at x_1 and x_2 , is given by a projection $k_\chi = k(\omega) \cdot \chi$, where $\chi = x_2 - x_1$. Essentially, all required information is contained in the cross-spectral density, $H(\chi, \omega)$, which is defined as:

$$H(\chi, \omega) = \lim_{T \rightarrow \infty} \frac{1}{T} \langle \tilde{B}^*(x_1, \omega) \tilde{B}(x_2, \omega) \rangle, \quad (2)$$

where T is the total time of the measurements and the angular brackets represent time averages. Expressing the complex quantity $H(\chi, \omega)$ in polar representation, allows the definition of the local wave number, k_χ in terms of the phase: $\Theta(\chi, \omega) = \text{Im}(H(\chi, \omega)) / \text{Re}(H(\chi, \omega))$,

$$k_\chi(\omega) = \frac{d}{d\chi} \Theta(\chi, \omega) \approx \frac{\Theta(\omega)}{\chi}. \quad (3)$$

In order to resolve a dispersion relation of multiple co-existing branches, it is necessary to calculate k_χ for an ensemble of data sets. Accordingly, for each interval in table I, the data is partitioned into N overlapping realisations of length T , chosen to include time scales of interest. The quantities given in (2) and (3) are then calculated for each realisation. This yields the local joint wavenumber-frequency spectrum

$$\hat{S}(k_\chi, \omega) = \langle \frac{1}{2} (|\tilde{B}(x_1, \omega)|^2 + |\tilde{B}(x_2, \omega)|^2) \delta(k - k_\chi) \rangle. \quad (4)$$

where angular brackets now indicate an ensemble average. A histogram of discrete cells in k and ω for $\hat{S}(k_\chi, \omega)$

is constructed to give the dispersion relation. Equation (4) converges to a real dispersion relation provided the plane wave approximation (1) is valid and that $k \cdot \chi < 2\pi$. The quantity $\hat{S}(k_\chi, \omega)$ is then a discrete two-dimensional histogram of the cumulative power on a (k_χ, ω) plane in the spacecraft reference frame.

In order to identify dispersion relations in the plasma rest frame, we apply the Doppler shift to (ω, k_χ) pairs which correspond to the maxima in $\hat{S}(\omega)$ at each frequency. In practice, we find three highest values of power, because some peaks may be over-resolved for a given number of bins in wave number and give the same Doppler shifted dispersion as the first maximum, for some frequencies. The procedure is then as follows: we identify three highest values of power in $\hat{S}(\omega)$ at each frequency, associate each frequency with its corresponding wave number k_χ and Doppler shift these using the mean solar wind velocity, that is:

$$\omega_{pl} = \omega_{sc} - k_\chi \langle V_{sw} \rangle \cos(\Theta_{v, \chi}). \quad (5)$$

We have chosen the convention whereby ω is always positive and we therefore switch the sign of the wave number $k_\chi \rightarrow -k_\chi$ when Doppler shifted frequency $\omega_{pl} < 0$. Finally, we choose a sign of k_χ in GSE coordinate system, that is, $k_\chi > 0$ for waves travelling Sunwards and $k_\chi < 0$ for waves travelling towards the bow shock in the plasma rest frame.

IV. RESULTS AND DISCUSSION

The two panels of Figure 2 show images of the cumulative power, \hat{S} , on the $(\omega_{sc}/\omega_{cp}, k_\chi \rho_i)$ plane, where ρ_i is the ion gyro-radius calculated using the CIS-HIA measured perpendicular temperature (with respect to magnetic field) and proton mass. The Nyquist frequency of the magnetic field measurements is 12.5 Hz, but we only show frequencies where some correlation of ω_{sc} and k_χ clearly exists. Beyond this range turbulent fluctuations dominate, producing a random, broad signature, without any apparent features. Wave number space in the range allowed by the method, that is $(-\pi/\chi, +\pi/\chi)$, which in SI units corresponds to wave length between $(-2.5, 2.5) \times 10^4$ meters, has been divided into 130 equally spaced bins. We note that the colour scale used in the figure is that of $\log_{10}(\hat{S})$. These plots were generated using ~ 100 strongly overlapping ($\sim 75\%$ overlap) realisations, each 5 minutes long. The data for each realisation has been detrended and we subtracted the mean prior to obtaining the Fourier components. The figure demonstrates that a clear wave activity can be found when applying the method outlined above, but strong Doppler shift obscures any details of the dispersion relations.

As outlined before, we find the three highest local maxima in \hat{S} and apply the Doppler shift to each identified $(\omega_{sc}/\omega_{cp}, k_\chi \rho_i)$ pair, as given in (5). These dispersion relations, in normalised quantities, are shown in figure 3

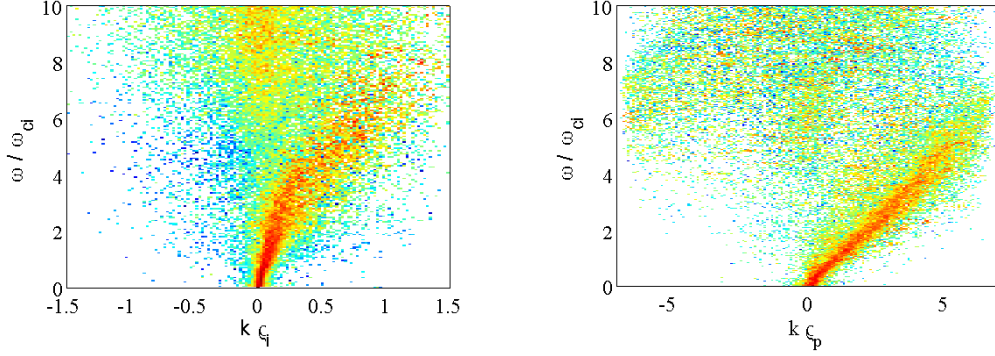


FIG. 2: Histograms of normalised cumulative power on normalised frequency-wave number plane for each interval.

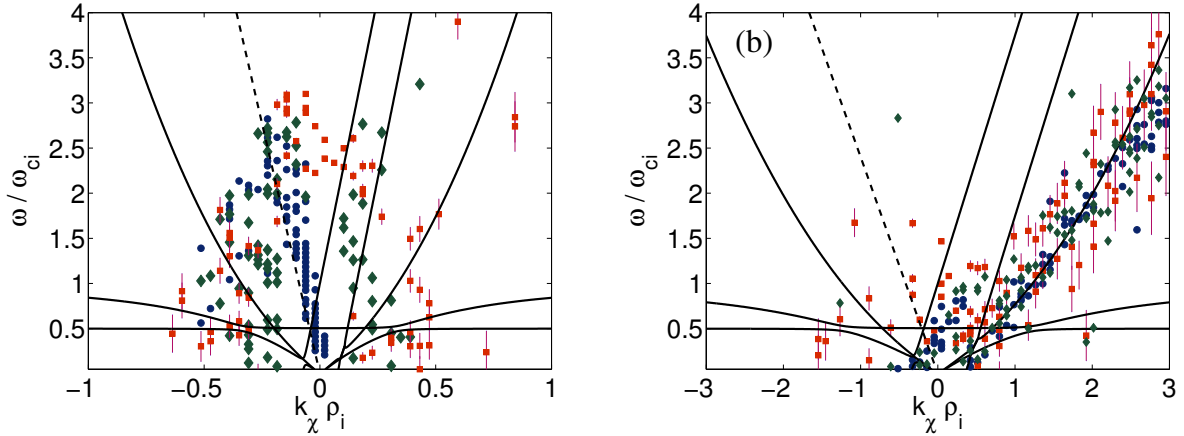


FIG. 3: Doppler shifted estimates of dispersion relations obtained for each interval (solid points) and cold plasma dispersion relations as a function of wave vector amplitude (solid lines). Symbols correspond to different maxima in fluctuation power in \hat{S} (see figure 2): the first maximum (highest power for a given frequency) is shown as circles, the second maximum is shown as diamonds and the third as squares. In panel (b) diamond symbols have been removed for clarity, they follow the same pattern as filled circles. Errors are from the Doppler shift uncertainty.

for each interval. Solid lines represent the cold plasma dispersion relations with massless electrons, background protons, background He^{++} ions and a proton beam [29]. We have used the wave propagation angle (w.r.t magnetic field vector) of 10° and beam velocity of $4.25V_A$ for $I1$ and the angle of 30° and $5V_A$ for $I2$, where V_A is the average Alfvén speed. The beam velocity and the wave propagation angle were not derived from the data, but were chosen based on the visual agreement of the theoret-

ical dispersion curves with experimental observations. In this context, the theoretical curves are given to guide the eye, but should not be compared directly to the discrete points, since k_χ is a projection of the estimated wave vector on the spacecraft separation vector and its true angle to the magnetic field is not known. Different symbols used in the figure correspond to the power associated with the local maxima in \hat{S} , filled circles represent the highest power, filled diamonds and squares correspond

to the second and the third peak, respectively. The errors shown are due to the uncertainty in the Doppler shift with the turbulent velocity field and have been calculated based on the variance of the solar wind velocity.

There is a clear difference between the two intervals considered here. For the interval *I1*, the most powerful fluctuations (filled circles) are convected structures, for which Taylor hypothesis is approximately satisfied, that is $\omega_{pl} \approx k_{\chi} V_{sw}$ (dashed line). A small fraction of the most powerful fluctuations is also positioned near the fast magnetosonic and Alfvén branch of the dispersion curves, for $k_{\chi} < 0$. These are waves travelling towards the bow shock and are most likely associated with the solar wind fluctuations. The points obtained from the secondary and the tertiary peak in power, shown as diamonds and squares, respectively, are equally distributed between fast magnetosonic and Alfvén modes propagating towards and away from the bow shock as well as the beam resonant mode. We have measured the ratio of power for the two dominant peaks, as a function of frequency, $PR(\omega) = \hat{S}(\omega)/\hat{S}_{max}(\omega)$. We found that this ratio shows a large increase around $\omega \approx 0.5\omega_{cp}$, so that $PR(\omega < 0.5\omega_{cp}) = 0.02$, while $PR(\omega > \omega_{cp}) = 0.6$. The largest k_{χ} value obtained for the Sunward propagating Alfvén branch ($k_{\chi} > 0$) is approximately $k_{\chi}\rho_p = 0.5$, which is much larger than the numerically found value for the most unstable left and right-hand polarised mode driven by cold beam [21]. Finally, we note a suggestive presence of points near the ion cyclotron branch of helium, He^{++} for *I1*. This branch is difficult to study, since the lower frequency modes require longer realisations to be considered. However, for the plasma that supports Bernstein modes, the minor ion resonance can contribute to magnetoacoustic cyclotron instability [38].

We contrast this with the finding from interval *I2*, where all three most powerful modes are predominantly these of the right-hand polarised fast magnetosonic type, propagating Sunwards. We note the presence of points along the straight solid line for $\omega < 0$ and $k_{\chi} < 0$, which coincide with the low frequency proton beam resonant modes. Similar to the previous interval, the secondary and tertiary populations, appears to follow the He^{++} cyclotron branch for modes propagating Sunwards, some of them have $k_{\chi}\rho_p \ll 1$, which may indicate a large perpendicular wave number component. Finally, some residual amount of power is found in the modes propagating towards the bow shock. This result while consistent with the previous analysis of this interval [14], supports numerical results which indicate that the unstable modes associated with the “diffused” ion population are both left and right-hand polarised modes propagating Sunward. We attribute residual power in the anti-Sunward propagating modes with the solar wind population.

Having established signatures of multiple dispersion relations in each interval we now examine proton distribution functions. Figure 4 shows CODIF proton pitch angle versus energy particle flux distributions, observed within ≈ 25 seconds window in intervals *I1* (top panel) and

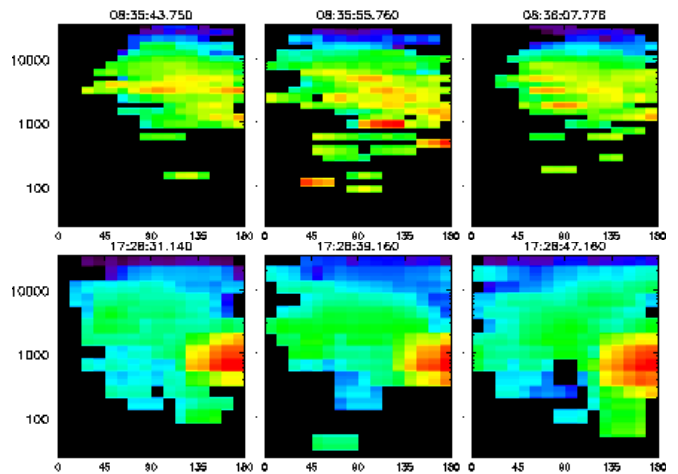


FIG. 4: Differential proton flux (colour scale), calculated from high resolution HIA proton spectra, for the total energy as a function of pitch angle for approximately 1 minute period within each studied interval. Horizontal axis gives pitch angle in degrees, vertical one shows the energy in eV.

I2 (bottom panel), respectively. While this observation window is very short compared with the total length of data, we have checked by visual inspection that these distributions provide a good representation of the ion population observed throughout each interval. CIS instruments were in the solar wind mode for interval *I1*, and in the magnetospheric mode during the second interval, *I2*. In the magnetospheric mode the instrument samples all angular directions and it is clear that the solar wind beam dominates the spectrum in this case. Accounting for this operational effect, both intervals show relatively typical shell-like ion distributions characteristic of the quasi-parallel foreshock. In both cases the peak ion energies are few keV and the distributions have some angular asymmetries. The CIS-CODIF spectra show low level of the solar wind flux contamination for the interval *I1*, with the warm proton beam at energy of about 10 keV.

V. CONCLUSIONS

We have identified multiple dispersion relations co-existing within the turbulent plasma for two different crossings of the terrestrial foreshock by Cluster spacecraft. These dispersions span beyond typically studied ULF waves in frequencies and wave numbers, with the maximum angular frequency exceeding the proton gyro-frequency by a factor of up to four. Constructed dispersion relations differ strikingly for the two intervals we have studied. Interval *I1*, while dominated by advocating structures, has significant amount of power in Alfvén and fast magnetosonic waves propagating in Sunward and unit-Sunward directions. Examined distribution functions show a typical “diffused” ions with energy

around 10 keV. While for highly anisotropic beam temperatures ($T_{\perp,b} > T_{\parallel,b}$) the instability can generate ion cyclotron waves propagating parallel and anti-parallel to the magnetic field [21], we must also admit a possibility that the anti-Sunward propagating fluctuations are these embedded in the solar wind. Importantly, the presence of counter-propagating Alfvén modes may give rise to their nonlinear interaction. We have already highlighted a possibility of ion cyclotron modes of He^{++} and their importance for the magnetoacoustic cyclotron instability.

Interval I2 shows the dispersion relation dominated almost entirely by fast magnetosonic and resonant proton beam modes, indicating an instability of the cold ion beam, for which $\omega_{pl} = k_{\parallel}v_b - \omega_{cp}$, where v_b is the speed of

the beam. While observed distribution functions for this interval show a typical “diffused” population, the instrument mode of interval I2 is dominated by the solar wind beam and is difficult to interpret. Previous study of this interval concluded that the observed fast magnetosonic waves are due to cold beam instability, since there is evidence that the observed dispersion includes beam resonant modes [14]. The right-hand polarised waves of the interval I2 reach speeds of up to $v_{ph}^R \approx 170$ km/s.

Acknowledgments: We acknowledge the CLUSTER team for data provision. This work was supported by the UK STFC and EU Marie Curie “Turboplasmas” funding.

-
- [1] Bell, A. R. (1978), Monthly Notices of the Royal Astronomical Society, 182, 147
 - [2] Leroy, M. M. (1983), Phys. Fluids, 26, 2742.
 - [3] Quest, K.B., Theory and Simulation of Collisionless Parallel Shocks, JGR, 101, 93, 9649-9680, 1988.
 - [4] Gosling, J. T., M. F. Thomsen, S. J. Bame, W. C. Feldman, G. Paschmann, and N. Sckopke, Geophys. Res. Lett., 9, 1333, 1982.
 - [5] Fairfield, D.H., JGR, 74, 3541, 1969.
 - [6] Gosling, J. T., J. R. Asbridge, S. J. Bame, G. Paschmann, and N. Sckopke, Geophys. Res. Lett., 5, 957, 1978.
 - [7] Paschmann, G., N. Sckopke, I. Papamastorakis, J. R. Asbridge, S. J. Bame, and J. T. Gosling (1981), J. Geophys. Res., 86(A6), 4355-4364, doi:10.1029/JA086iA06p04355.
 - [8] Tu, C.-Y., and E. Marsch, J. Geophys. Res., 99(A11), 21481-21509 (1994) doi:10.1029/94JA00843.
 - [9] Xin Wang, Jiansen He, Chuanyi Tu, Eckart Marsch, Lei Zhang, and Jih-Kwin Chao, Astroph. Journal, 746, 147 (2012).
 - [10] Bruno, R. and Carbone, V., Living Reviews in Solar Physics, 2 (2005).
 - [11] Justin C. Kasper, Bennett A. Maruca, Michael L. Stevens, and Arnaud Zaslavsky Phys. Rev. Lett. 110, 091102 (2013).
 - [12] R. O. Dendy, C. N. Lashmore-Davies, K. G. McClements, and G. A. Cottrell, Physics of Plasmas 1, 1918 (1994); doi: 10.1063/1.870647
 - [13] E. A. Lucek, T. S. Horbury, A. Balogh, I. Dandouras, and H. Réme, Annales Geophysicae (2004) 22: 2309-2314
 - [14] Y. Narita, K.-H. Glassmeier, S. Schafer, U. Motschmann, K. Sauer, I. Dandouras, K.-H. Fornacon, E. Georgescu, and H. Réme, Geophys. Res. Lett., 30, 1710, doi:10.1029/2003GL017432, 2003.
 - [15] Y. Narita, K.-H. Glassmeier, S. Schafer, U. Motschmann, K. Sauer, I. Dandouras, K.-H. Fornacón, E. Georgescu, and H. Réme and I. Richter, Annales Geophysicae (2004) 22: 2315-2323
 - [16] Hoppe, M. M., and C. T. Russel, J. Geophys. Res., 88, 2021-2028 (1983).
 - [17] Le, G., Generation of upstream ULF waves in the Earth's foreshock, PhD Thesis, University of Calif., Los Angeles, 1991.
 - [18] Winske D., Leroy M. M., JGR 89, 2673 (1984).
 - [19] A. N. Fazakerley, A. J. Coates and M. W. Dunlop, Adv. Space Res., 15, 103-106, 1995.
 - [20] Eastwood, J.P., Balogh, A., Lucek, E.A., Ann. Geophys., 21, 1457-1465, 2003
 - [21] Gary, S.P., ApJ, 288, 342-352, 1985.
 - [22] Sentman, D.D, Edmiston, J.P., & Frank, L., JGR, 86, 7487, 1981.
 - [23] Balogh, A., Dunlop, M. W., Cowley, S., et al., SSRv, 79, 65, 1997.
 - [24] Réme, H., Ann. Geophys., 19, 1303-1354, 2001.
 - [25] Hollweg, J. V. (1994), J. Geophys. Res., 99(A12), 23431-23447, (1994) doi:10.1029/94JA02185.
 - [26] J. M. Beall, Y. C. Kim, and E. J. Powers, J. Appl. Phys. 53, 3933 (1982); doi: 10.1063/1.331279
 - [27] Dudok de Wit, T., Krasnoselskikh, V. V., Bale, S. D., Dunlop, M. W., Luhr, H., Schwartz, S. J., and Woolliscroft, L. J. C., Geophys. Res. Lett., 22, 2653-2656, 1995.
 - [28] M. A. Balikhin, L. J. C. Woolliscroft, H. St. C. Alleyne, M. Dunlop, M. A. Gedalin, Ann. Geophysicae 15, 143-151 (1997).
 - [29] Daniel Verscharen and Benjamin D. G. Chandran, The Astrophysical Journal 764, 88 (2013).
 - [30] Gary, S.P., Li, H., O'Rourke, S., & Winske, D., JGR, 103, 14, 567-14, 574, 1998.
 - [31] Hoppe, M. M., C. T. Russell, T. E. Eastman, and L. A. Frank, J. Geophys. Res., 87, 6436-50, doi:10.1029/JA087iA02p00643, 1982
 - [32] L. A. Selzer, B. Hnat, K. T. Osman, V. M. Nakariakov, J. P. Eastwood, and D. Burgess, The Astroph. J. Lett. 788, Number 1 (2014).
 - [33] X. Blanco-Cano and S. J. Schwartz, Ann. Geophysicae 15, 273-288 (1997).
 - [34] Marsch, E., Ao, X.Z., & Tu, C.Y., JGR, 109, A04102, 2004.
 - [35] Quest, K.b., & Shapiro, V.D., JGR, 101, 24, 457-24, 469, 1996.
 - [36] Rosin, M.S., Schekochihin, A.A., Rinson, F., & Cowley, S.C., Mon. Not. R. Astron. Soc, 413, 7, 2011.
 - [37] Russell, C.T., Childers, D.D, & Coleman, P., JGR, 76, 845, 1971.
 - [38] R. O. Dendy, C. N. Lashmore-Davies, K. G. McClements, and G. A. Cottrell, Physics of Plasmas 1, 1918 (1994); doi: 10.1063/1.870647